



Tang, H., Tao, W., Wang, H., Song, Y., Jian, X., Yin, L., ... Scarpa, F. (2018). High-performance infrared emissivity of micro-arc oxidation coatings formed on titanium alloy for aerospace applications. *International Journal of Applied Ceramic Technology*, 15(3), 579-591.
<https://doi.org/10.1111/ijac.12861>

Peer reviewed version

Link to published version (if available):
[10.1111/ijac.12861](https://doi.org/10.1111/ijac.12861)

[Link to publication record in Explore Bristol Research](#)
PDF-document

This is the author accepted manuscript (AAM). The final published version (version of record) is available online via Wiley at <https://onlinelibrary.wiley.com/doi/abs/10.1111/ijac.12861>. Please refer to any applicable terms of use of the publisher.

University of Bristol - Explore Bristol Research

General rights

This document is made available in accordance with publisher policies. Please cite only the published version using the reference above. Full terms of use are available:
<http://www.bristol.ac.uk/pure/about/ebr-terms>

High-performance infrared emissivity of micro-arc oxidation coatings formed on titanium alloy for aerospace applications

Hui Tang ^{a, b, c, d*}, Wei Tao ^a, Hong Wang ^a, Yuanqiang Song ^a, Xian Jian ^a, Liangjun Yin ^a, Xin Wang ^{b, c}, Fabrizio Scarpa ^{e*}

- a. School of Energy Science and Engineering, University of Electronic Science and Technology of China, Chengdu, 610000, China
- b. National Engineering Research Center of Electromagnetic Radiation Control Materials, University of Electronic Science and Technology of China, Chengdu, 610054, China
- c. State Key Laboratory of Electronic Thin Films and Integrated Devices, University of Electronic Science and Technology of China, Chengdu, 610054, China
- d. School of Chemical Engineering and Technology, Harbin Institute of Technology, Harbin 150001, China
- e. Bristol Composites Institute (ACCIS), University of Bristol, BS8 1TR Bristol, UK

Abstract

Aerospace vehicles are subjected to high temperatures because of surrounding aerodynamic drag and the formation of large temperature gradients across the external structural parts of their airframe. To protect the vehicles, high infrared emissivity coatings that can radiate a large amount of heat into outer space are in demand. In this work we describe the development and characterization of high emissivity ceramic coatings formed on a TC4 alloy surface by micro-arc oxidation. We evaluate, in particular, the influence of NiSO₄ concentration on current-time response, the

*Corresponding author: Hui Tang, Tel/fax: 86-028-61831326, E-mail: tanghui@uestc.edu.cn
Fabrizio Scarpa, E-mail: F.Scarpa@bristol.ac.uk

thickness, surface roughness, morphologies, bonding strength and emissivity of these coatings. The results indicate that by increasing the NiSO_4 concentration in electrolytes, the thickness and surface roughness of the coatings increase. The bonding strength becomes smaller with increasing concentration of NiSO_4 , but is still maintains a value higher 30 MPa. The coatings possess good thermal shock resistance after being subjected to severe thermal shocks for 50 cycles, and no peeling of the coating is observed. A higher concentration of NiSO_4 in electrolytes also leads to an increasing percentage of the nickel components in the coating to form a NiO phase, which enhances the emissivity of the coatings in the wavelength range of 3-8 μm .

Keywords: Microarc oxidation; Titanium alloy; Nickel sulfate; Bonding strength; High emissivity

1. Introduction

Titanium (Ti) alloys are materials extremely attractive for aerospace applications because of their unique and excellent combinations of strength to weight ratio and resistance to corrosion [1, 2]. For structure applications in hypersonic vehicles, surfaces made of Ti alloys, however, suffers from severe aerodynamic heating during hypersonic flight. The friction caused by the aerodynamic drag generates a dramatic increase of the surface temperature, and therefore tends to deteriorate the overall thermo-mechanical performance of the materials [3, 4]. As a consequence, there is a strong demand in the industry for a coating targeted at Ti alloys that can radiate a large amount of heat in the surrounding space [5]. A conventional technique to fabricate high-emissivity coating is based on the use of brushes [6]. Infrared radiative

materials, with inorganic binders, are usually brushed onto the surface of metals. Depositing high-emissivity materials by brush is simple, however this technique leads to coatings with low adhesion strength and poor thermal shock resistance. The use of brushing is therefore severely limited for large-scale applications in the aerospace field [7]. Several surface treatment techniques have been developed to develop high emissivity coatings on titanium alloys and improve the adhesion strength and the thermal shock resistance of the coatings. Amongst several surface treatment methods, one has to mention thermal and plasma spraying, as well as electron beam physical vapor deposition for the production of high-emissivity coatings [8-10]. However, these particular techniques are difficult to apply in several cases. For example, uniform thickness coatings on a substrate with complex geometry are difficult to obtain by using thermal and/or plasma spraying, and also by adopting electron beam physical vapor deposition techniques. In addition, the costs associated to the production of coatings with these types of techniques are still considerable. Therefore, the availability of a facile, controllable and cost-effective technique for high-emissivity coatings is one of the priorities for high-performance airframe constructions.

Micro-arc oxidation (MAO) is considered to be a convenient and effective technique to produce high-quality ceramic coatings on Ti and its alloys [11]. MAO is suitable to deposit over various substrates with complex geometries, and MAO-derived coatings generally exhibit good bonding strength and thermal shock resistance [12, 13]. Wang *et al.* [14] have assessed the bonding strength and infrared

emissivity properties of MAO coatings with TiO_2 , and observed some general improvements of these two properties after applying a two-steps MAO process. In this particular type of two-steps production, it is widely believed that the electrolyte composition can greatly influence the properties of the MAO coatings formed on titanium based metals [15]. Yao *et al.* [16] have also added high emissive components in the electrolyte that were supposed to massively improve the emissivity of MAO coatings, however the results are still somehow inconclusive.

Nickel oxide-based thin films/coatings have been developed on various substrates due to their intrinsiching infrared emissivity and good thermal oxidation resistance [17]. Studies on nickel oxide-based thin films have been developed for a wide number of applications, ranging from energy savings for industrial furnaces, to selective solar thermals, and spacecraft thermal control [18]. Nickel oxide-based composite films have the potential to provide high emissivity and constant thermo-mechanical properties at high temperatures. In this work, NiSO_4 is added to the electrolyte to fabricate nickel oxide-based coatings on TC4 titanium alloy by using the MAO technique. We also evaluate the bonding strength and the thermal shock resistance of these novel coatings. We demonstrate that the manufacturing process we develop represents an effective and convenient meth to produce high-emissivity coatings for broad range applications in the aerospace industry.

2. Manufacturing and methods

TC4 titanium discs with a diameter of 30 mm and thickness of 6 mm have been used here as the substrate. The discs have been grounded first with SiC papers, then

ultrasonically cleaned in ethanol for 10 min and finally dried. The discs were then used as anodes. A home-made pulsed electrical source of 20 kW was used for the micro-arc oxidation of the samples in a water-cooled electrolyzer made of stainless steel, which also served as a cathode. The reaction temperature was controlled to below 30 °C by adjusting the flow of the cooling water. The electrolyte was prepared by boiling redistilled water and adding the appropriate amount of NiSO₄ to achieve 0, 1, 3 and 5 g/L concentrations. The corresponding as-fabricated samples were labeled as MAO0, MAO1, MAO3 and MAO5. Then, 9 g/L of Na₃PO₄ were also added to the solutions. During the MAO treatment a constant voltage mode was applied. The anodic voltage was kept constant at 400 V, while the cathodic voltage was controlled at 0 V. The frequency of the voltage excitation was 100 Hz, and the MAO treatment lasted for 20 mins.

Scanning electron microscopy (SEM, S-4800, Hitachi Co., Japan) was used to investigate the surface and the morphologies of the section of the coatings. The distribution of elements on the surface of the coating was evaluated by using energy dispersive spectroscopy (EDS, Oxford Model 7537, England). The phase composition of the coatings was examined using a RICOHD/max-rB automatic X-ray diffractometer (XRD, D/max-rB, Japan) using a Cu K α source. The XPS measurements were performed using a commercial PHI 5700 apparatus (America Physical Electronics, USA). The base pressure in the analytical chamber was 10⁻⁷ Pa, with a monochromated Al K α X-ray source present (1486.6 eV). The high-resolution XPS spectra used for the assessment of the chemical state and its quantification were

recorded at constant pass energy of 20 eV. The data analysis and the quantification were carried out using the software provided by the manufacturer. The roughness of the coatings was measured with a current-based roughness gauge (TR-200, Time Company). The average roughness of each sample was obtained from eight measurements at different positions. The thickness of the coating was measured by, using an eddy current-based thickness gauge (CTG-10, Time Company).

The bonding strength of the coatings was evaluated in an adhesion-tension test according to ASTM-C633 standard [19]. The average bonding strength of the five samples was acquired by treating all the specimens under the same conditions. It is worth noticing that the coatings on one side of the samples were removed, and the exposed Ti alloy surface was then roughened. The two sides of the samples were then attached to cylindrical steel jigs with a diameter of 10 mm by using epoxy glue. The tensile load was applied to the samples with an Instron-type testing machine at a speed of 1 mm/min until fracture occurred. The fracture surfaces were examined by SEM to determine where fracture occurred. The thermal shock resistance of the coatings was investigated through a cyclic heating-cooling test. Two types of experiments were carried out with each MAO-coated sample. In the first experiment the samples were heated to a temperature of 500 °C and with a dwell time of 5 mins in air, and then placed for 1 min in room temperature water. In the second experiment the specimens were this time heated to up to 700 °C, exposed to for 5mins, and then again placed in a container with water at room temperature for 1 min. The tests were repeated for 50 cycles, and the coating surface was visually inspected to identify

whether cracks or large area flakes were produced. The infrared emissivity of the samples was measured using an in-house infrared radiometer made at Harbin Institute of Technology. The radiation emitted by the sample front surface was detected by a Fourier transform infrared (FT-IR) spectrometer wavelength range of 3-20 μm , and its radiance was compared with one of a reference blackbody radiator.

3. Results

3.1 Current-time response

During MAO processes, the voltage was scanned with a rate of 4 V/s until it reached 400 V, and then was then kept constant. Fig. 1 shows the current to time curves of the titanium alloy coated in electrolytes with the four different NiSO_4 concentrations. For all of the samples, the trends of the current history are the same. In these current histories five phases can be clearly identified. Initially the current increases at a high rate in region a, while for increasing voltages the same current tend to decrease in region b. Within region c, a large number of small sized sparks can be observed, with the presence of white light scanning over the surface of the titanium alloy. The current increases again, but with a softening effect over time compared to region a. The current reaches maximum value at 400 V, then quickly decreases in region d. In this phase some quick movements of orange/red sparks over the surface of the titanium alloy have been observed. Within region e, the current drops slowly and reaches a relatively stable value. In this stage the sparks become more pronounced and are accompanied with intense productions of gas. It is apparent that the increased concentration of NiSO_4 in the electrolyte is responsible

for the increased current rates in region a, but also for the maximum value of the current in region c, and the current in region e. This indicates that higher energy occurs during the MAO process for increasing concentrations of NiSO_4 in the electrolyte, and these higher energy levels lead to an increase of the intensity of the spark discharge. As the NiSO_4 concentration increased, larger and longer-lived spark discharges were actually observed.

Fig. 1. Current-time curves obtained for coatings with different NiSO_4 solutions

3.2 Thickness and roughness of the MAO coatings

The measured coating thickness and surface roughness of the samples made from different NiSO_4 concentrations in electrolytes are shown in Fig.2. The thickness and roughness of the MAO coatings increases with increasing NiSO_4 concentration. The thickness of the coatings is 5.6, 6.5, 7.6 and 7.9 μm when the concentration of NiSO_4 is 0, 1, 3 and 5 g/L, respectively. The thickness of the coatings tends to increase sensibly for concentrations below 3 g/L, while for higher concentrations the increase of thickness is less noticeable. An opposite behavior is however observed for the surface roughness, which tends to be not very sensitive to increase in smaller NiSO_4 concentrations (below 3 g/L). For 5 g/L NiSO_4 solution, the roughness of the coatings showed a sharp increase and this indicates that the concentration of NiSO_4 in the electrolyte used in the MAO process has a strong effect on the growth of the oxide.

Fig. 2. Variation of the thickness and roughness of the MAO coatings formed

with different NiSO_4 solutions

3.3 Surface morphologies and elemental ratio of the MAO coatings

The surface morphologies of the MAO coatings produced for various NiSO_4 concentrations are shown in Fig. 3. All of the coatings have porous microstructures with different pores dimensions and distributions. The MAO0 coating has a large number of evenly distributed pores within the range of 0.5-1.5 μm . The MAO1, MAO3 and MAO5 show different surface textures compared to the MAO0 one. Two distinct characteristics on the surfaces can be clearly identified. The first are the so-called sintered protrusions with relatively large-sized micropores (regions in red circles), and the other is a surface with numerous smaller micropores. With increasing concentration of NiSO_4 , the number of sintered protrusions and the size of the micropores on the surface increase, while the surface of the MAO5 coating is dominated by sintered protrusions features.

As shown in the previous studies [20], the formation of micropores is due to the emission of gas bubbles and molten oxide trapped in the growing coating. These emissions escape through the micro-arc discharge channels. The different surface morphologies of the coatings can also be attributed to the different discharge characteristics during the MAO process. In addition, the number and size of the pores depend on the energy density during the sparking discharge. Higher energy densities induce larger discharge sparks and form larger sections of molten oxide. The larger pores and larger sintered granules remain afterwards on the surface. Hence, the energy density increase with increasing concentration of NiSO_4 is responsible for the larger

pores and larger sintered granules on the surface of the MAO coatings formed at higher NiSO_4 concentrations.

Fig. 3. Surface morphologies of the MAO coatings formed with different NiSO_4 additions of: (a) MAO0, (b) MAO1, (c) MAO3, and (d) MAO5

The relative contents of the elements in the coating are shown in Table 1. The presence of Ni and P in the MAO coating suggests that the electrolyte species penetrate into the oxide coating during the MAO process. Titanium from the metal substrate is found to present inside the coatings. The EDS results however show that sulfur was not present on the surface of the coatings, as sulfur could have potentially been removed as SO_2 gas from the electrolyte. Based on the atomic ratio measured during the EDS tests one can conclude that the Ni/Ti ratio is increased with more nickel incorporated into the coatings with increasing of NiSO_4 concentrations.

Table 1 Elemental contents of the MAO coatings formed with different NiSO_4 concentrations

3.4 Cross-section morphologies and elemental distribution

SEM observations were conducted on polished cross sections of the MAO samples mounted in epoxy resin. The cross-sectional morphology of the MAO3 coating is shown in Fig. 4a. It can be observed that the thickness of the coating is approximately 8 μm . The MAO coating appears to integrate closely with the titanium

substrate through interlocking, which implies the presence of a good bonding between the coating and the substrate itself.

An EDS line scan was used to investigate the elemental distribution within the cross-section of the MAO3 coating (Fig. 4b). Elements like Ti, Al, O, P, and Ni have been detected within the coating. The presence of phosphate increased rapidly near the interface of the substrate/inner oxide film, from the substrate to the coating. The opposite happened for the titanium, which tended to decrease rapidly within the same region of the coating. Nickel increased gradually, with the highest concentration present on the surface of the outer part. This behavior is explained by the fact that nickel must move to the interface of the coating/electrolyte and enter into the coating. From the inside to outside of the coating, the quantity of oxygen was gradually reduced, whereas the concentration of aluminum was almost constant within the coating.

Fig. 4. Cross-section morphology and elemental distribution of the MAO3 coating

3.5 Phase and chemical composition of the coatings

Fig. 5 shows the XRD patterns of MAO0, MAO1, MAO3 and MAO5. The coatings are composed of rutile and anatase TiO_2 , but their ratio varies with different concentrations of NiSO_4 in the electrolyte. More rutile and less anatase are formed in the presence of higher concentrations of NiSO_4 . Peaks conforming to the titanium substrate also appear in the patterns. No peaks corresponding to Ni and P elements are however detected, possibly due to their existence in the coatings amorphous phase

Fig. 5. XRD patterns of the coatings with different NiSO₄ additions

We employed the XPS technique to investigate the surface chemical composition of the MAO coatings. The results were interpreted according to the C (1s) core level bonding energy at 284.6 eV. The XPS investigation was performed on the MAO3 coating, which alone because it showed a more consistent phase structure and topography. The XPS survey scan of the surface of the MAO3 is shown in Fig. 6. The coating contains mainly titanium, aluminum, oxygen, phosphate and nickel and these results. This consistent with the one measured during the EDS tests.

Fig. 6. XPS scan of the MAO3 coating surface

Fig. 7 shows the Ni2p, Ti2p, P2p and O1s XPS spectra belonging to the surface of the MAO3 coating. The Ni2p^{3/2} and Ni2p^{1/2} core level binding energy are deconvoluted into two distinct components (Fig. 7a). This feature demonstrates the presence of two different Ni bindings in the coating. The peaks of Ni2p^{3/2} located at the binding energy of 856.8 eV [21] and of Ni2p^{1/2} at 871.8eV [22], verify the existence of NiO within the coating. The core level of Ni2p^{3/2} was at 858.6 eV and at 873.7 eV for Ni2p^{1/2}. These combinations of levels and binding energy demonstrate the existence of Ni(OH)₂ [23]. Fig. 7b shows the Ti2p^{3/2} and Ti2p^{1/2} core levels at binding energies of 458.9 and 464.8 eV, corresponding to TiO₂ [24]. Within the P2p spectrum one can be observe the presence of a single peak detected at 133.3 eV (Fig. 7c). It can be therefore concluded that the P element exists in the coating in the form of a phosphate group [25]. Fig. 7d shows the presence of the O1s peak, which can be

deconvoluted this time into three components, indicating the existence of three different oxygen bindings at the surface of the coating. The peak located at a binding energy of 532.4 eV corresponds to oxygen in metaphosphate (P-O-P, P-O-M) [26]. A peak at approximately 531.2 eV is attributed, on the other hand, to oxygen within the hydroxyl groups (-OH) [27]. The oxide peak around 529.6 eV is symptomatic of TiO₂ and NiO [28]. The peaks of Ni2p^{3/2} and Ni2p^{1/2} indicate that the Ni²⁺ in the electrolyte was incorporated into the coatings during the MAO process, and formed NiO and Ni(OH)₂ [29-32].

The coating composition can therefore be expressed as a mixture of different possible compounds, like titanium dioxide, nickel oxide, and nickel hydroxide with a small sodium phosphate contribution. Sodium phosphate may become trapped in the coating and is not washed away completely.

Fig. 7. XPS spectra of the MAO3 coating at the (a) Ni 2p, (b) Ti 2p, (c) P 2p, and (d) O 1s core level binding energies

3.6 Adhesion behavior

The adhesion strength of a coating with a substrate is a critical factor for the mechanical integrity of the coating system and it significantly affects the long-term stability of the protection coating. Fig. 8a shows the variation of the bonding strength between the MAO coatings and the titanium alloy substrate for different NiSO₄ concentrations. The bonding strengths of all of the coatings are higher than 30 MPa. The average value of the bonding strength appears to decrease slightly with increasing

NiSO₄ concentrations in the electrolytes. The coatings produced using MAO grow as a result of a plasma chemical oxidation reaction of the substrate near the electrolyte, and do not contain an “artificial” interface as deposited coatings. Therefore, the adhesion strength is expected to be relatively high.

Fig. 8b shows a typical morphology of the fractures surface after the bonding test. The outer layer of the coating is pulled off, and this is an indication that the failure occurs within in the coating. The cohesive strength of the coating is therefore lower than the bonding strength between the coating and the substrate.

Fig. 8. Bonding strength and typical fracture surface of the MAO coatings formed with different NiSO₄ solutions

3.7 Thermal shock resistance of the coatings

The thermal shock resistance of the coating is a key factor for high-end aerospace applications. After severe thermal shock with temperatures up to 500 °C and 700 °C for 50 cycles, no peeling off of the coating has been observed by visual inspection, which indicates that the coating possesses a good thermal shock resistance. Further SEM observations of MAO3 coating surface morphologies after thermal shock tests are shown in Fig. 9. It is evident from the two pictures of the Figure that no change takes place after the 500 °C thermal shock test, however some micro-cracks appear after the 700 °C thermal shock test. Some cracks are located in areas with pores, while others are present in non-pore areas bridging, some cracks together. The cracks however do not appear to compromise significantly the structural integrity of the coating. Furthermore, no peeling off of the coating can be observed though the SEM pictures. These features give evidence that the coating possesses some rather

good thermal shock resistance properties and adhesion strength to the substrate.

Fig. 9. Typical morphologies of the coatings after thermal shock at: (a) 500 °C for 50 cycles and (b) 700 °C for 50 cycles

3.8. Emissivity characterization

Fig. 10 shows the spectral emissivity measured within the wavelength range of 3-20 μm at 700 °C for the titanium substrate and the MAO coatings. The titanium substrate shows a significantly lower infrared emissivity of approximately 0.3 in the 3-8 μm range, and 0.36 in 8-14 μm band. It can be also observed that the MAO coatings exhibit a higher infrared emissivity in the wavelength range of 3-20 μm . In the wavelength range of 3-8 μm , the infrared emissivity of the MAO coatings increases with increasing NiSO_4 concentration in the electrolytes. The infrared emissivity of the MAO0 coating has however an abrupt increase within the 8.2-9.5 μm wavelength range. The emissivity of the MAO0 coating is higher than those of the MAO1 and MAO3 ones in the 9.5-12 μm band, whereas within the 12-20 μm wavelength range the emissivity is almost the same for the MAO0, MAO1 and MAO3 coatings. The spectral emissivity of the coatings reaches its maximum at a wavelength of approximately 7.4 μm , and the position of the dominant peak shows very little change with the NiSO_4 concentration in the electrolytes. The coating prepared in the electrolyte without NiSO_4 however does not exhibit a clearly dominant peak. The MAO5 coating possesses the highest infrared emissivity value in the 3-20 μm wavelength range. Within the 3-8 μm band the emissivity of the MAO5 coating is

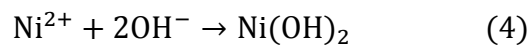
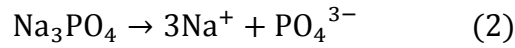
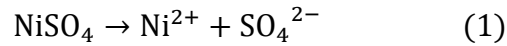
between 0.75-1, and has a maximum value of 1 for a wavelength of 7.4 μ m. The average infrared emissivity of the MAO5 coating is larger than 0.9 within the 8-20 μ m range.

Fig. 10. Spectral emissivity of the substrate and the MAO coatings with different NiSO₄ concentrations

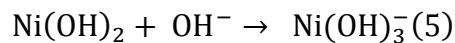
4. Discussions

4.1 Mechanisms underlying the oxidation during the MAO process

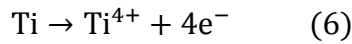
As NiSO₄ is added to the electrolyte solution, complex chemical reactions occur like, ionization, and hydration reactions. The main reactions occurring during the process are:



NiSO₄ and Na₃PO₄ in water can be ionized, and form nickel, sodium ion, sulfate, and phosphate ions. The phosphate then reacts with water and releases hydroxyl. The nickel ion can bond with hydroxyl and form nickel hydroxide. In addition, the alkaline environment leads to nickel hydroxide further reducing the surface energy by absorbing negative ions such as OH⁻. The nickel hydroxide particles are therefore negatively charged.



During the MAO process, the high voltage applied generates an electric field between the anode and cathode. The field ensures that the negatively charged ions migrate towards the titanium anode, and the positively charged ones to the cathode. Owing to the different ionic radius and ion mobility, the surface of the titanium anode is encapsulated by hydroxyl, and then phosphate and sulfate. The distribution of these ions is illustrated in Fig. 11a. The ion layer over the titanium surface is mainly composed of hydroxyl groups. The next ion layer is mainly constituted by phosphate, sulfate, and hydrogen phosphate ions. Nickel hydroxide particles are also located near the anode, but they concentrate on the surface of the ion layer. During the MAO process, Ti^{4+} is formed by dissolution of the titanium from the substrate under the effect of the electric field.



The formation of uniform granular products on the titanium alloy is attributed to the outward migration of Ti^{4+} and inward migration of OH^- , PO_4^{3-} , SO_4^{2-} , HPO_4^{2-} , and $\text{Ni}(\text{OH})^{3-}$ under the effect of a high voltage potential. Film formation reactions occur, when these ions enter the reaction interface. Because of the different distributions of the negatively charged ions on the surface anode, the OH^- group has priority in reacting with Ti^{4+} . The other groups (PO_4^{3-} , SO_4^{2-} , and HPO_4^{2-}) then join the coating. The last one to join is $\text{Ni}(\text{OH})^{3-}$ (Fig. 11b). Owing to the complex reactions, the elements originate from the electrolyte and the substrate is absorbed into the coating. The coating can be also be thought as being divided into three layers (Fig. 11c). The first layer from the substrate is mainly composed of oxygen and titanium. The second

layer is mainly composed of O, Ti and P. The composition of the third layer is similar to the second one, with added nickel this time. The distribution of the elements in the coating is in agreement with the results from the EDS line scan (Fig. 4b).

Fig. 11. Schematic diagram of the formation mechanism of the MAO coatings

4.2 Current distribution during the MAO process

It is well known that many chemical and physical reactions, like chemical, electrochemical and plasma oxidations are involved within the MAO process because high voltage and current density are applied [33]. The electrolytes also take part in the reactions, rather than just provide an electrolysis environment. Several previous studies [34, 35] have focused on the influence of the additives and on the voltage history in constant current MAO process. A common outcome of these studies is the discovery that the variations of the voltage can be associated to three stages: anodic oxidation, breakdown and micro-arc oxidation. In this study we have performed a constant voltage mode MAO process, and the current history can be now divided into five regions depending on the type of variation of the current. The changes of the current-time patterns presented in Fig. 1 can be interpreted by considering the specific physical and chemical reactions occurring in the MAO process, which are described as follows. During the first stage the voltage is below the breakdown voltage, and the process is therefore a conventional anodic oxide one. The Ti alloy substrate is dissolved first, and metal shine is lost. Subsequently a thin barrier layer is formed on the sample surface, but this little influence on the current. According to Ohm's law,

the current increases linearly with increasing voltage, and it exhibits a nearly linear increase within region a. With increasing voltage the thickness of the anodic oxidation film increases rapidly, and impedes the passage of current through the film (decrease in region b). Within the region c the current increases again, because the film is breaking down. Following the Ikonopisov model [36], if the applied voltage is sufficiently high, an avalanche of electrons at the interface between the electrolytes and oxide layers would pass through the film. And cause the film to breakdown, thus making the current increase quickly. Within region d, a steady-state sparking state is established on the anodic surface. White sparks change into isolated orange ones that move slowly across the surface. In this process, the thickness of the MAO coating increases rapidly, which leads to the current decreasing sharply in this phase. Finally, within region e the current decreases slowly due to the relatively steady rate of growth of the coating layer.

During the whole MAO process the electrolyte and the film can be considered as two parts of a series circuit (Fig. 12). Thus, the resistance and the applied voltage can be expressed as:

$$R_t = R_s + R_f \quad (7)$$

Where R_t is the total resistance of the electrochemical cell, R_s is the electrolyte electrical resistance and R_f is the resistance of the film. When a voltage is applied to the circuit, it is expressed as

$$U_t = U_s + U_f \quad (8)$$

Where U_t is the total voltage applied to the circuit, U_s is voltage applied to the

electrolyte and U_f is the voltage applied to the film. It is known that the resistance of the electrolyte decreases with increasing concentration of additives. And therefore the total resistance of the electrochemical cell decreases with increasing NiSO_4 concentrations. The decrease of the circuit resistance results in increased current passing through the cell. As it can be observed from Fig. 1, the rate of the current within region an increases with increasing concentration of NiSO_4 in the electrolyte. When the resistance of the electrolyte decreases the voltage applied to the anode surface becomes larger, and more electric avalanches occur. Therefore, the maximum value of the current occurs in region c, and the final quasi stable value of the current in region e increases with increasing concentrations of NiSO_4 . This also results in larger remnant discharge channels on the surface of the oxide coatings, as shown in Fig. 2.

Fig. 12. Equivalent circuit for the MAO coating formation process

4.3 Influence of NiSO_4 on the emissivity

The emissivity is a property that reveals the radiation quantity that a given body emits compared to the one of a blackbody. The emissivity is highly influenced by the state of the surface state (i.e., surface roughness and presence of inorganic components). According to the general theory of scattering, rougher surfaces result in higher emissivity of the coating [37]. The infrared emissivity measured over the wavelength range of 3-7.4 μm for the MAO3 and MAO5 coatings are shown in Fig. 12. Considering the large difference in terms of roughness, one can however notice a

small variation of the infrared emissivity for the two coatings. There is however a very small difference between the roughness of the MAO1 and MAO3 coatings, and the infrared emissivity of MAO3 is significantly higher than the one exhibited by the MAO1 coating. Our results are in agreement with data previously obtained by Wang *et.al.* [38]. The roughness has little influence on the infrared emissivity values of the MAO coatings, because of their special porous structure that causes reflectance of the infrared thermal wave inside the pores, but not on the surface of the coatings.

NiO ceramic has been reported to possess a higher infrared emissivity than TiO₂ in the wavelength range of 3-8 μm [39]. It is therefore expected to obtain higher emissivity value by adding NiO. The MAO coating formed without NiSO₄ is mainly composed by TiO₂, and the coating possesses a limited infrared emissivity within the 3-8 μm wavelength range. In comparison, the coatings produced in the NiSO₄ electrolytes consist of both TiO₂ and NiO, and the amount of NiO increases with increasing concentration of NiSO₄. The coating produced with higher NiSO₄ concentrations have as a consequence higher emissivity values over 3-8 μm due to the increasing NiO content.

5. Conclusions

High infrared emissivity coatings have been prepared on TC4 titanium alloy by micro-arc oxidation with different NiSO₄ concentrations in the electrolyte. The structure, phase composition, chemical state, bonding strength and thermal shock resistance of the coatings have been investigated and the following conclusions can be drawn:

(1) For all of the samples, the trend of the current-time curves is the same, and five regions can be identified depending on the increase of the current during the MAO process.

(2) The concentration of nickel sulfate affects considerably the morphologies, as well as the phase components, thickness and roughness of the coatings. When the nickel sulfate concentration increases, the coating becomes thicker and rougher, and contains more rutile titanium dioxide and nickel oxide. Larger pores can be observed with increasing concentrations of nickel sulfate in the electrolytes, which lead to increasing currents in the MAO process.

(3) The bonding strength of the coatings decreases with increasing nickel sulfate concentrations, however all coatings show a bonding strength higher than 30 MPa. After severe thermal shocks performed for 50 cycles, no peeling off of the coating has been observed, demonstrating good thermal shock resistance.

(4) The infrared emissivity of the coatings is improved by adding nickel sulfate to the electrolytes. The infrared emissivity of the coatings in the 3-8 μm wavelength range increases with increasing nickel sulfate concentrations.

The coatings developed in this work show a significant potential in high-end aerospace applications where the protection of the air frame surface is paramount.

Acknowledgements

This research was supported by the National Natural Science Foundation of China (Grant No.51402045). And Central University basic research business expenses (No.ZYGX2014J089).

References

1. Chowdhury MSI, Chowdhury S, Yamamoto K, et al. Wear behaviour of coated carbide tools during machining of Ti6Al4V aerospace alloy associated with strong built up edge formation, *Surf. Coat. Technol.* 2017; 313:319-327.
2. Banerjee D, Williams JC, Perspectives on Titanium Science and Technology, *Acta Mater.* 2013; 61:844-879.
3. Satko DP, Shaffer JB, Tiley JS, et al. Effect of microstructure on oxygen rich layer evolution and its impact on fatigue life during high-temperature application of α/β titanium, *Acta Mater.* 2016; 107:377-389.
4. Huda Z, Edi P, Materials selection in design of structures and engines of supersonic aircrafts: A review, *Mater. Des.* 2013; 46:552-560.
5. Wang C, Hao JM, Xing YZ, et al. High temperature oxidation behavior of $\text{TiO}_2 + \text{ZrO}_2$ composite ceramic coatings prepared by microarc oxidation on Ti6Al4V alloy, *Surf. Coat. Technol.* 2015; 261:201-207.
6. Shao GF, Lu YC, Wu XD, et al. Preparation and thermal shock resistance of high emissivity molybdenum disilicide- aluminoborosilicate glass hybrid coating on fiber reinforced aerogel composite, *Appl. Surf. Sci.* 2017; 416:805-814.
7. Curry N, Tang ZL, Markocsan N, et al. Influence of bond coat surface roughness on the structure of axial suspension plasma spray thermal barrier coatings-Thermal and lifetime performance, *Surf. Coat. Technol.* 2015; 268:15-23.
8. Dhineshkumar SR, Duraiselvam M, Natarajan S, et al. Enhanced ablation

- resistance through laser glazing of plasma sprayed $\text{LaTi}_2\text{Al}_9\text{O}_{19}$ -based functionally graded thermal barrier coating, *Ceram. Int.* 2016; 42:10184-10190.
9. Klyatskina E, Rayón E, Darut G, A study of the influence of TiO_2 addition in Al_2O_3 coatings sprayed by suspension plasma spray, *Surf. Coat. Technol.* 2015; 278:25-29.
 10. Goral M, Kotowski S, Nowotnik A, et al. PS-PVD deposition of thermal barrier coatings, *Surf. Coat. Technol.* 2013; 237:51-55.
 11. Li H, Sun YZ, Zhang J, Effect of ZrO_2 particle on the performance of micro-arc oxidation coatings on Ti6Al4V , *Appl. Surf. Sci.* 2015; 342:183-190.
 12. Li QB, Yang WB, Liu CC, et al. Correlations between the growth mechanism and properties of micro-arc oxidation coatings on titanium alloy: Effects of electrolytes, *Surf. Coat. Technol.* 2017; 316:162-170.
 13. Friedemann AER, Gesing TM, Plagemann P, Electrochemical rutile and anatase formation on PEO surfaces, *Surf. Coat. Technol.* 2017; 315:139-149.
 14. Wang ZW, Wang YM, Liu Y, et al. Microstructure and infrared emissivity property of coating containing TiO_2 formed on titanium alloy by microarc oxidation. *Curr. Appl. Phys.* 2011; 11:1405-1409.
 15. Wang YH, Ouyang JH, Liu ZG, et al. Microstructure and high temperature properties of two-step voltage-controlled MAO ceramic coatings formed on Ti_2AlNb alloy. *Appl. Surf. Sci.* 2014; 307:62-68.
 16. Yao ZP, Hu B, Shen QX, et al. Preparation of black high absorbance and high emissivity thermal control coating on Ti alloy by plasma electrolytic oxidation.

- Surf. Coat. Technol. 2014; 253:166-170.
17. Beshkar F, Zinatloo-Ajabshir S, Salavati-Niasari M, Simple morphology-controlled fabrication of nickel chromite nanostructures via a novel route, Chem. Eng. J. 2015; 279:605-614.
 18. Zhang JY, Fan XA, Lu L, et al. Plasma sprayed ferrite-based infrared radiation coating directly from transition metal oxides without high-temperature roasting, Mater. Lett. 2015; 61:348-351.
 19. Tang H, Han Y, Wu T, et al. Synthesis and properties of hydroxyapatite-containing coating on AZ31 magnesium alloy by micro-arc oxidation, Appl. Surf. Sci. 2017; 400:391-404.
 20. Jr ES, de Souza GB, Serbena FC, et al. Effect of anodizing time on the mechanical properties of porous titania coatings formed by micro-arc oxidation, Surf. Coat. Technol. 2017; 309:203-211.
 21. Li ZF, Dong HP, Zhang YL, et al. Enhanced removal of Ni (II) by nanoscale zero valent iron supported on Na-saturated bentonite, J. Colloid Interface Sci. 2017; 497:43-49.
 22. Keraudy J, Ferrec A, Richard-Plouet M, et al. Nitrogen doping on NiO by reactive magnetron sputtering: A new pathway to dynamically tune the optical and electrical properties, Appl. Surf. Sci. 2017; 409:77-84.
 23. Adán-Más A, Duarte RG, Silva TM, et al. Enhancement of the Ni-Co hydroxide response as Energy Storage Material by Electrochemically Reduced Graphene Oxide, Electrochim. Acta. 2017; 240:323-340.

24. Wang SX, Zhao Q, Liu DX, et al. Microstructure and elevated temperature tribological behavior of $\text{TiO}_2/\text{Al}_2\text{O}_3$ composite ceramic coating formed by microarc oxidation of Ti6Al4V alloy, *Surf. Coat. Technol.* 2015; 272:343-349.
25. Lee JH, Youn J, Kim YJ, et al. Photocatalytic characteristics of boron and nitrogen doped titania film synthesized by micro-arc oxidation, *Ceram. Int.* 2015; 41:11899-11907.
26. Zhang XT, Hang RQ, Wu HB, et al. Synthesis and antibacterial property of Ag-containing TiO_2 coatings by combining magnetron sputtering with micro-arc oxidation, *Surf. Coat. Technol.* 2013; 235:748-754.
27. Zhu L, Zeng YQ, Zhang SL, et al. Effects of synthesis methods on catalytic activities of $\text{CoO}_x\text{-TiO}_2$ for low-temperature $\text{NH}_3\text{-SCR}$ of NO, *J. Environ. Sci.* 2017; 54:277-287.
28. Yang ZD, Wei XJ, Gao W, et al. Anodization of NiTi alloy in an ethylene glycol electrolyte, *Surf. Coat. Technol.* 2014; 252:142-147.
29. Lukiyanchuk IV, Rudnev VS, Chernykh IV, et al. Composites with transition metal oxides on aluminum and titanium and their activity in CO oxidation, *Surf. Coat. Technol.* 2013; 231:433-438.
30. Sharma A, Lee BK, Integrated ternary nanocomposite of TiO_2/NiO /reduced graphene oxide as a visible light photocatalyst for efficient degradation of *o*-chlorophenol, *J. Environ. Manage.* 2016; 181:563-573.
31. Coviello D, Contursi M, Toniolo R, et al. Electrochemical and spectroscopic investigation of a binary Ni-Co oxide active material deposited on

- graphene/polyvinyl alcohol composite substrate, *J. Electroanal. Chem.* 2017; 791:117-123.
32. Mohammadloo HE, Sarabi AA, Titanium composite conversion coating formation on CRS In the presence of Mo and Ni ions: Electrochemical and microstructure characterizations, *Appl. Surf. Sci.* 2016; 387:252-259.
 33. Tang H, Gao Y, Preparation and characterization of hydroxyapatite containing coating on AZ31 magnesium alloy by micro-arc oxidation, *J. Alloys Compd.* 2016; 688:699-708.
 34. Ko YG, Namgung S, Shin DH, Correlation between KOH concentration and surface properties of AZ91 magnesium alloy coated by plasma electrolytic oxidation, *Surf. Coat. Technol.* 2010; 205:2525-2531.
 35. Polat A, Makaraci M, Usta M, Influence of sodium silicate concentration on structural and tribological properties of microarc oxidation coatings on 2017A aluminum alloy substrate, *J. Alloys Compd.* 2010; 504:519-526.
 36. Mi T, Jiang B, Liu Z, et al. Plasma formation mechanism of microarc oxidation. *Electrochim. Acta.* 2014; 123:369-377.
 37. González-Fernández L, Risueño E, Pérez-Sáez RB, et al. Infrared normal spectral emissivity of Ti-6Al-4V alloy in the 500-1150 K temperature range. *J. Alloys Compd.* 2012; 541:144-149.
 38. Bosta MMSA, Ma KJ, Chien HH, The effect of MAO processing time on surface properties and low temperature infrared emissivity of ceramic coating on aluminium 6061 alloy, *Infrared Phys. Technol.* 2013; 60:323-334.

39. Tang H, Sun Q, Yi CG, et al. High emissivity coatings on titanium alloy prepared by micro-arc oxidation for high temperature application, J. Mater. Sci. 2012; 47:2162-2168.

Figure captions

Fig. 1. Current-time curves obtained for coatings with different NiSO_4 solutions

Fig. 2. Variation of the thickness and roughness of the MAO coatings formed with different NiSO_4 solutions

Fig. 3. Surface morphologies of the MAO coatings formed with different NiSO_4 additions of: (a) MAO0, (b) MAO1, (c) MAO3, and (d) MAO5

Fig. 4. Cross-section morphology and elemental distribution of the MAO3 coating

Fig. 5. XRD patterns of the coatings with different NiSO_4 additions

Fig. 6. XPS scan of the MAO3 coating surface

Fig. 7. XPS spectra of the MAO3 coating at the (a) Ni 2p, (b) Ti 2p, (c) P 2p, and (d) O 1s core level binding energies

Fig. 8. Bonding strength and typical fracture surface of the MAO coatings formed with different NiSO_4 solutions

Fig. 9. Typical morphologies of the coatings after thermal shock at: (a) 500 °C for 50 cycles and (b) 700 °C for 50 cycles

Fig. 10. Spectral emissivity of the substrate and the MAO coatings with different NiSO_4 concentrations

Fig. 11. Schematic diagram of the formation mechanism of the MAO coatings

Fig. 12. Equivalent circuit for the MAO coating formation process

Table 1Table 1 Elemental contents of the MAO coatings formed with different NiSO₄

concentrations				
	0g/L	1.0g/L	3.0g/L	5.0g/L
Ni		3.61	11.74	14.57
Ti	27.01	25.17	20.93	18.56
P	19.90	17.00	16.90	17.44
O	53.09	54.23	50.43	49.39
Ni/Ti	0	0.14	0.56	0.78